



Cite this: *RSC Adv.*, 2017, 7, 29806

# Electrospun TiO<sub>2</sub>/ZnO/PAN hybrid nanofiber membranes with efficient photocatalytic activity

Adem Yar,<sup>a</sup> Bircan Haspulat,<sup>b</sup> Tugay Üstün,<sup>a</sup> Volkan Eskizeybek, <sup>\*c</sup> Ahmet Avcı,<sup>a</sup> Handan Kaniş<sup>b</sup> and Slimane Achour<sup>d</sup>

Electrospun polyacrylonitrile (PAN) nanofibers were decorated with TiO<sub>2</sub>, ZnO and TiO<sub>2</sub>/ZnO nanoparticles for the first time to prepare flexible multifunctional nanofibrous membranes. First, the arc-discharge process was utilized to prepare TiO<sub>2</sub>, ZnO and TiO<sub>2</sub>/ZnO nanoparticles and then the hybrid electrospun nanofibers were spun from PAN/nanoparticle colloids. X-ray diffraction, scanning electron microscopy (SEM) and transmission electron microscopy (TEM) were utilized to characterize the resulting nanoparticles and nanofiber loaded nanoparticles. The microscopic investigations revealed that the specifically TiO<sub>2</sub> nanoparticles tend to agglomerate within the PAN nanofiber resulting increased surface roughness; however, ZnO nanorods with 1D morphology are aligned as parallel to the fiber axis. Photocatalytic activity of the hybrid nanofibers was performed by pursuing the degradation of malachite green (MG) dye under UV light irradiation. The fabricated TiO<sub>2</sub>/ZnO/PAN hybrid nanofibers showed excellent photocatalytic efficiency with at least two times higher reaction rates compared to the bare PAN nanofibers. The results suggest that the photocatalytically active TiO<sub>2</sub>/ZnO/PAN hybrid nanofibers can be considered as filtering materials for a variety of applications in the fields of wastewater systems without the need of post processing stages for separating catalysts from the liquid medium.

Received 31st March 2017  
Accepted 1st June 2017

DOI: 10.1039/c7ra03699j

rsc.li/rsc-advances

## 1. Introduction

Treatment of wastewater in the industries like pharmaceuticals, textile, leather, chemicals, and petroleum, *etc.* is required to decompose organic dyes.<sup>1</sup> Different water treatment and purification methods,<sup>2–4</sup> are often utilized to remove dyes from liquid environments due to associated serious health issues<sup>5</sup> and environmental problems. Photocatalytic approaches are increasingly being addressed to develop less expensive,<sup>6</sup> low energy consumption, high efficiency, and a practically advanced oxidization technique for disposal of the pollutants.<sup>7,8</sup> Improving photocatalytic activity by modifying the catalyst has been an active research area in the past decade.<sup>9</sup> Researchers have expressed various methods, such as doping transition metals<sup>10</sup> and non-metals,<sup>11</sup> and forming composite photocatalysts from different semiconductors,<sup>12</sup> *etc.*, to enhance the photocatalytic activity of nanocatalysts. The results reveal that nearly all composite semiconductors have higher photocatalytic activity than a single semiconductor. Zinc oxide (ZnO) is a wide bandgap semiconductor (3.37 eV) with a 60 meV exciton binding energy, which permits laser emission at room

temperature. This large band gap is suitable for the use of ZnO to collect high-energy photons (UV light) as a photocatalyst in environmental cleaning.<sup>13</sup> Titanium(IV) dioxide (titania) is an important transition metal oxide, widely used as a catalyst support, semiconductor photocatalyst, and gas and humidity sensor.<sup>14</sup> Titania exists in three crystal forms as rutile, anatase, and brookite. Thermodynamically stable rutile phase of titania has a tetragonal structure with 3.0 eV band gap of the bulk which is smaller than anatase phase. In some cases, rutile was found to be more active for photocatalysis.<sup>15</sup>

Up until now, in most photocatalysis studies, post-treatment removal of semiconducting photocatalyst after photocatalytic reaction can be a difficult, time-consuming and costly process.<sup>16</sup> Alternatively, the catalyst may be immobilized on a suitable solid inert support with the desired morphology, to eliminate post processes for removing the catalyst.<sup>17</sup> Among these forms, the nanotube and nanofiber with the 1-D characteristic, which is to have one dimension many times longer than the other ones, are of particular interest. These structures provide high effective surface area and a defined flow pattern along the longer dimension, which greatly contribute to the enhanced photocatalytic efficiency in practical applications. In addition, flexibility and elasticity need to be other essential features of the next generation of photocatalysts. The electrospinning is regarded as a versatile and effective approach to prepare organic flexible nanofibrous mats with tunable diameters due to its advantages of ease of control and environmental compatibility.<sup>18,19</sup> The

<sup>a</sup>Department of Mechanical Engineering, Selçuk University, Konya, Turkey

<sup>b</sup>Department of Chemical Engineering, Selçuk University, Konya, Turkey

<sup>c</sup>Department of Materials Science and Engineering, Çanakkale Onsekizmart University, Çanakkale, Turkey. E-mail: veskizeybek@comu.edu.tr

<sup>d</sup>Ceramic Laboratory, University of Constantine, Algeria


electrospun polyacrylonitrile (PAN) filament forming mats, may be promising as a template polymer for the immobilization of catalytic materials due to their hydrophobic and flexible nature with too low density.<sup>20</sup> Therefore, it easily floats on the liquid. This point would make the ability of photodegradation maximized with optimized irradiation efficiency of UV light by avoiding the hindrance of UV source penetration.<sup>21</sup>

The goal of this study to develop efficient nanofibrous membranes using a scalable process with eliminating the need for post-processing stages of separating catalysts from the liquid medium after degradation of organic dyes. Therefore, we have successfully achieved PAN based electrospun nanocomposite fibers loaded with ZnO and TiO<sub>2</sub> nanoparticles. The electrospun fibers were utilized to decolorize an organic dye under UV light irradiation. The results showed that the obtained nanofibers with high surface area exhibit a good photocatalytic activity.

## 2. Materials and methods

The proposed methodology for preparation and characterization of the PAN based nanocomposite spun fiber mats contains two main fabrication processes as represented schematically in Fig. 1. In the first step, the arc discharge method was implemented to prepare ZnO, TiO<sub>2</sub>, and ZnO–TiO<sub>2</sub> nanostructures, following, PAN-based nanocomposite fibers were spun from PAN/nanoparticle polymer solution as the second step.

### 2.1 Materials

All chemicals were of analytical grade and used without further purification. High purity Zn and Ti rods (Alfa Aesar, 99.99%) were used as electrodes to synthesize ZnO, TiO<sub>2</sub>, and ZnO–TiO<sub>2</sub> nanoparticles. Dimethylformamide (DMF) and malachite green (MG) were purchased from Merck.

### 2.2 Synthesis of metal oxide nanoparticles

The metal oxide nanoparticles were synthesized by an arc discharge method in de-ionized water medium as described in

our previous studies.<sup>22–24</sup> Briefly, a voltage controlled arc discharge apparatus containing vertically aligned metal electrodes was submerged in the de-ionized water-filled vessel and the arc was generated between electrodes applying a fixed current. Note that, Ti and Zn rods were directly used as electrodes to synthesize TiO<sub>2</sub> and ZnO nanoparticles, respectively, however; Ti–Zn composite electrode was prepared to synthesize ZnO/TiO<sub>2</sub> nanocomposite structures. Namely, a hole with the same diameter of Zn rod was drilled through the pure Ti rod and the pure Zn rod was placed within the hole to produce concentric Ti–Zn composite rod acting as an anode during arc discharge process. Discharge voltage was measured and kept constant by controlling the gap between the metal electrodes to maintain stable arc discharge during the process. Anode electrode was consumed during the process and the resulted particles dispersed within the de-ionized water medium. The vessel was kept at room temperature for 24 h to complete settling of the synthesized nanostructures. The settled particles were collected carefully by decanting and centrifuging of the suspensions, subsequently. Finally, the collected nanostructures were washed with de-ionized water and absolute ethanol and dried at 40 °C under vacuum for 24 h.

### 2.3 Fabrication of hybrid nanofiber

Electrospinning technique was utilized to fabricate PAN based nanocomposite fiber mats. Similar to our previous works,<sup>25,26</sup> 0.25 g of the arc discharge synthesized nanoparticles (TiO<sub>2</sub>, ZnO or TiO<sub>2</sub>/ZnO) were added into 12 mL DMF solution and the mixture was sonicated ultrasonically for 30 min. 1 g of PAN (8% w/v) was added to the homogenized mixture and mixed for 2 h at 60 °C to obtain proper viscosity for electrospinning. Then, the solution was transferred into a 10 mL syringe with a blunt-tipped 23-gauge needle. The distance between the needle tip and the square plate acting as a collector was adjusted as 15 cm. Feed rate of the polymer solution was kept constant during the spinning process as 0.15 mL h<sup>−1</sup>. The electric field occurred between the needle tip and the square plate was generated using a high voltage power supply with an applied voltage of 25

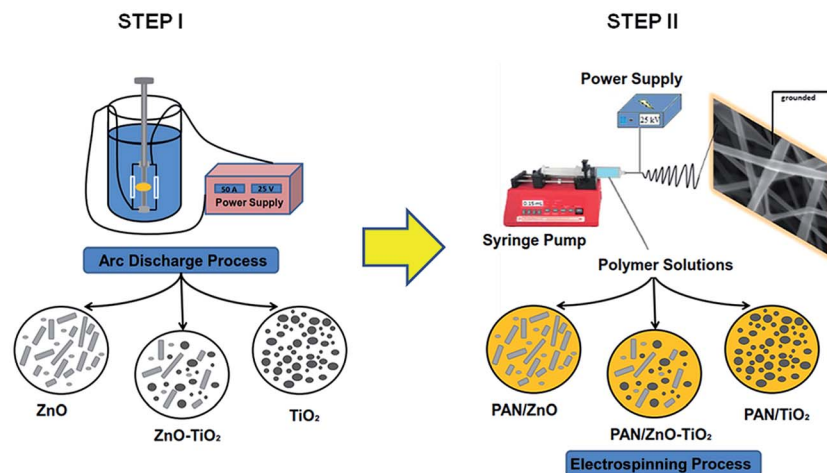


Fig. 1 The methodology used to fabricate PAN based electrospun fibers modified with ZnO, TiO<sub>2</sub> and ZnO–TiO<sub>2</sub> nanostructures.



kV. PAN/ZnO, PAN/TiO<sub>2</sub>, and PAN/ZnO/TiO<sub>2</sub> nanofibers were collected on the plate surface.

## 2.4 Characterization

XRD patterns of nanofibers were recorded with a Bruker Advance D8 XRD (Cu  $\alpha$  source with 1.5406 wavelengths) in powder mode. ZeissEvo scanning electron microscope (SEM) and JEOL 2100 transmission electron microscope (TEM) were used to obtain morphological and structural properties of the nanofibers. The FTIR spectra of all materials were recorded by a Perkin Elmer 1725 spectrophotometer.

## 2.5 Measurement of photocatalytic activity

Malachite green (MG, C<sub>23</sub>H<sub>25</sub>N<sub>2</sub>·C<sub>2</sub>H<sub>3</sub>O<sub>4</sub>·0.5C<sub>2</sub>H<sub>2</sub>O<sub>4</sub>) was used as a model dye to investigate the photocatalytic activity of electrospun PAN, PAN/TiO<sub>2</sub>, PAN/ZnO and TiO<sub>2</sub>/ZnO/PAN hybrid nanofiber. Photocatalytic decolorization of MG under UV light was carried out in a Luzchem model 4V photoreactor (Luzchem Research Inc., Canada) equipped with 2 UVC lamps with an emission at  $\lambda = 254$  nm. 1.2 mg of the electrospun nanoparticles were added into a quartz tube, and 3 mL of MG aqueous solution with the concentration of  $1.0 \times 10^{-5}$  M was introduced. This mixture was magnetically stirred for 30 min in dark to reach the adsorption-desorption equilibrium. Then UV lamps were switched on to start the photocatalytic decolorization of MG. The photocatalytic decolorization of MG was investigated at room temperature in the presence/absence of different catalysts under irradiation/dark for given times. The concentration of the MG dye was evaluated by using the UV-vis spectroscopy method. The degradation efficiency of dye is calculated by the following equation;

$$\text{Degradation (\%)} = \frac{C_0 - C}{C_0} \times 100$$

where  $C_0$  is the initial concentration of dye before irradiation and  $C$  is the concentration of dye after a certain irradiation time. In general, the photocatalytic degradation of organic pollutants on the semiconducting oxide can be ascribed to a pseudo-first-order reaction which follows the simplified Langmuir-Hinshelwood model;

$$-\frac{\ln C}{C_0} = kt$$

where  $C$  is the measured MG concentration at different intervals,  $C_0$  is the initial MG dye concentration measured after 30 min absorption and  $k$  refers to the reaction rate kinetic constant and  $t$  is the irradiation time.

## 3. Results and discussion

### 3.1 Structure and morphology

The XRD patterns of the arc discharge synthesized nanoparticles are represented in Fig. 2a. The diffraction peaks at 31.77°, 34.42°, 36.25°, 47.45°, 56.60°, and 62.86° are indicative of the typical hexagonal wurtzite ZnO phase (JCPDS no. 30-1451) while the main peaks at 27.7°, 36.1°, 41.4°, and 54.5°

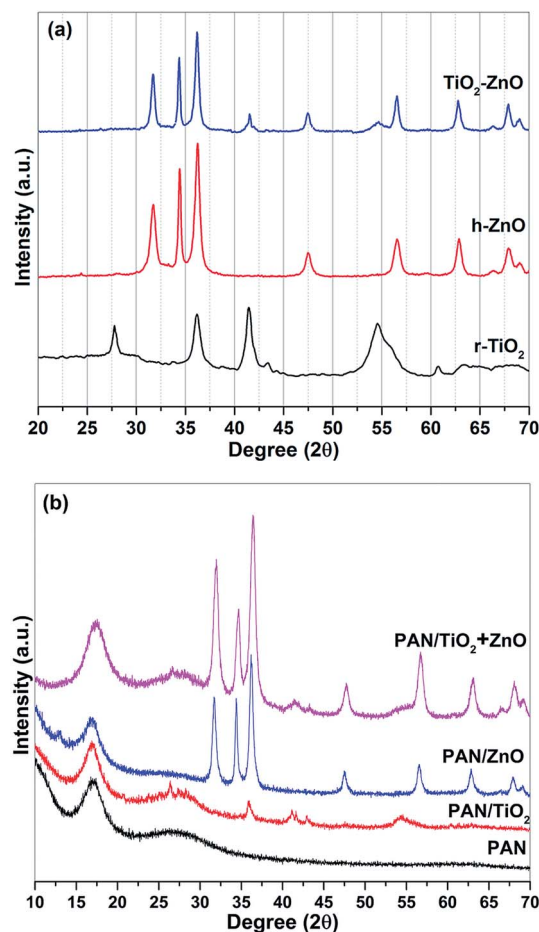


Fig. 2 XRD patterns of (a) nanostructures prepared via arc-discharge method showing rutile structure of TiO<sub>2</sub>, hexagonal wurtzite structure of ZnO and TiO<sub>2</sub>-ZnO nanocomposite structures, (b) PAN based nanocomposite electrospun fibers.

correspond to the XRD pattern of the rutile phase of TiO<sub>2</sub> (JCPDS no. 88-1175). The breadth and weakness of the TiO<sub>2</sub> peaks can be explained by the small grain sizes and amorphous/crystalline structure of the r-TiO<sub>2</sub> nanostructures. More details on the amorphous/crystalline structure are discussed in TEM analysis. The use of Zn-Ti composite electrode as an anode during arc discharge process resulted in a nanocomposite formation of ZnO/TiO<sub>2</sub> multiphase due to the appearance of h-ZnO and r-TiO<sub>2</sub> peaks on the same pattern.<sup>22</sup> No characteristic peaks other than h-ZnO and r-TiO<sub>2</sub> crystalline phase were appeared in the XRD pattern, implying the high purity of the as-synthesized nanostructures by arc discharge method. Similarly, XRD measurements were further utilized to examine the crystal structure of the electrospun nanocomposite fibers (Fig. 2b). PAN nanofiber exhibits two wider amorphous peaks appear in the ranges of 15 and 20°, 20 and 30° with a moderate degree of crystalline order.<sup>27,28</sup> Compared with the XRD curve of the pure PAN fibers, the hybrid electrospun nanofibers indicate crystal planes of the hexagonal wurtzite structure of ZnO and tetragonal rutile TiO<sub>2</sub> similar to that described in the literature.<sup>29,30</sup> The XRD curve of electrospun TiO<sub>2</sub>/ZnO/PAN nanocomposite





fibers represents both of the metal oxide phases with a slight shift to higher degrees.

Electron microscopy monitoring was also utilized to reveal morphologies and structures of the arc discharge synthesized nanostructures. TEM images of the ZnO, TiO<sub>2</sub> and ZnO/TiO<sub>2</sub> nanostructures are given in Fig. 3. The as-synthesized ZnO nanoparticles are almost in nanorod form (Fig. 3a) with diameters ranging from 10 to 30 nm and lengths range from 50 to 100 nm. The r-TiO<sub>2</sub> nanoparticles are in well spherical shape and the diameter of the nanospheres is ranging from 5 to 50 nm (Fig. 3b). The r-TiO<sub>2</sub> nanoparticles are in well spherical shape and the average particle size of r-TiO<sub>2</sub> nanoparticles was about 5–70 nm (Fig. 3b). The nanoparticle morphology and size distributions can be influenced by arc-discharge parameters.<sup>31</sup> In this case, it is quite difficult to control the continuity and stability of the arc-discharge process and therefore the process can result in nanoparticles with different size distributions.<sup>32</sup> In contrast, it is apparent that an amorphous shell with the non-uniform thickness (less than 5 nm) was formed around the r-TiO<sub>2</sub> nanoparticles. The structure in the shell of the present nanoparticles is different from the amorphous shell.<sup>33</sup> We believe that the occurrence of weak and breadth peaks of the as-synthesized r-TiO<sub>2</sub> nanospheres on the XRD spectrum directly related with this core-shell structure. Homogeneous distribution of the two phases (h-ZnO and r-TiO<sub>2</sub>) as ZnO–TiO<sub>2</sub> nanocomposite structures was acquired using a composite anode electrode with a combination of Zn and Ti rods during arc discharge process as visualized by a TEM analysis (Fig. 3c). It can be seen from the image that the as-synthesized ZnO–TiO<sub>2</sub> nanocomposite structure contains nanorods and nanospheres as two different nanostructure morphologies with similar sizes as observed during analysis of the individual phases.

Typical SEM images of the electrospun hybrid nanocomposite fibers were presented in Fig. 4. The randomly oriented PAN based nanofibers are mainly composed of well-defined smooth outer surfaces and beadles structure with lengths of several hundreds of micrometers to millimeters and diameters range from 50 to 400 nm (Fig. 4a). Incorporation of nanoparticle results in the particular coarseness and roughness of PAN nanofibers but with raised diameters compare to PAN nanofibers. Namely, the PAN nanocomposite fibers have rougher surfaces due to the presence of the TiO<sub>2</sub>, ZnO and TiO<sub>2</sub>/ZnO nanoparticles on the surface when compared to pristine

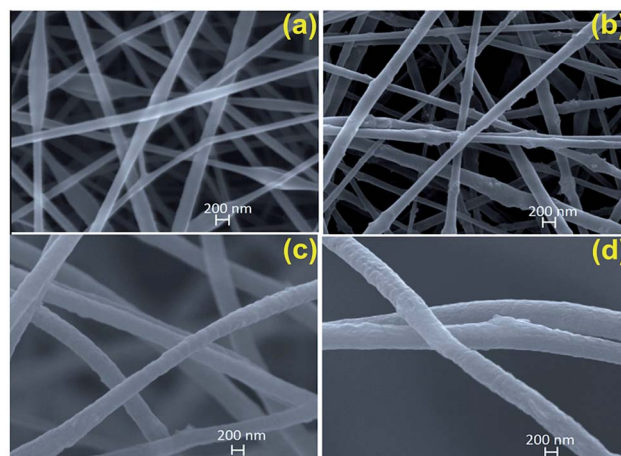


Fig. 4 SEM images of (a) pristine PAN nanofiber, (b) PAN/TiO<sub>2</sub> nanofiber, (c) PAN/ZnO and (d) TiO<sub>2</sub>/ZnO/PAN nanofibers.

PAN nanofibers (Fig. 4b–d). It is evident that the PAN/TiO<sub>2</sub> nanocomposite fibers exhibited highest surface roughness which is primarily the result of the highest agglomeration tendency of TiO<sub>2</sub> nanospheres due to their smaller sizes rather than ZnO nanoparticles. Moreover, the increment in diameter of nanofiber could be explained the increase in the viscosity of polymer solution due to the incorporation of the nanoparticle. As a result, the increase in polymer solution viscosity leads to an enlargeable and steady fiber diameter.<sup>34,35</sup> The EDS mapping of SEM was utilized to explore the presence of Ti and Zn nanoparticle in the nanofibers. Here, Fig. 5 presents EDS elemental maps for PAN/TiO<sub>2</sub>, PAN/ZnO, and TiO<sub>2</sub>/ZnO/PAN hybrid nanofibers. It is revealed that C, N, O, Ti and Zn are generally exhibited a homogenous and uniform distribution throughout the nanofibers and thereby proving the presence of Ti and Zn nanoparticles in the nanofibers.

The detailed microstructures of the electrospun hybrid nanofibers were further examined utilizing TEM as shown in Fig. 6. PAN nanofibers represent smooth surfaces and the measured diameters consist with the SEM results (Fig. 6a). The TEM image of PAN/TiO<sub>2</sub> nanofibers (Fig. 6b) represents a different morphology from the neat PAN nanofibers. TiO<sub>2</sub> nanoparticles agglomerated within the PAN fiber as the light areas indicate PAN nanofibers and the dark areas show the

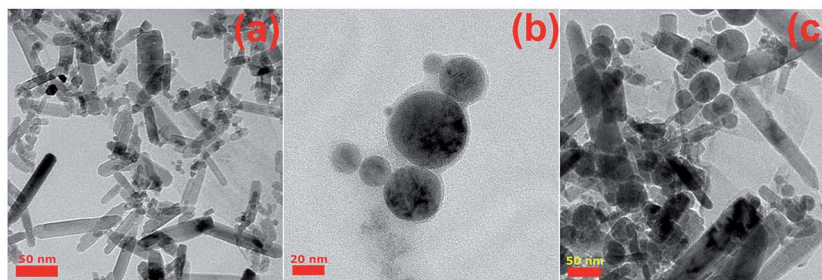


Fig. 3 Representative TEM images of (a) ZnO nanoparticles (scale bar 50 nm), (b)  $\alpha$ -TiO<sub>2</sub> nanospheres (scale bar 20 nm), (c) ZnO + TiO<sub>2</sub> nanocomposite structures (scale bar 50 nm).



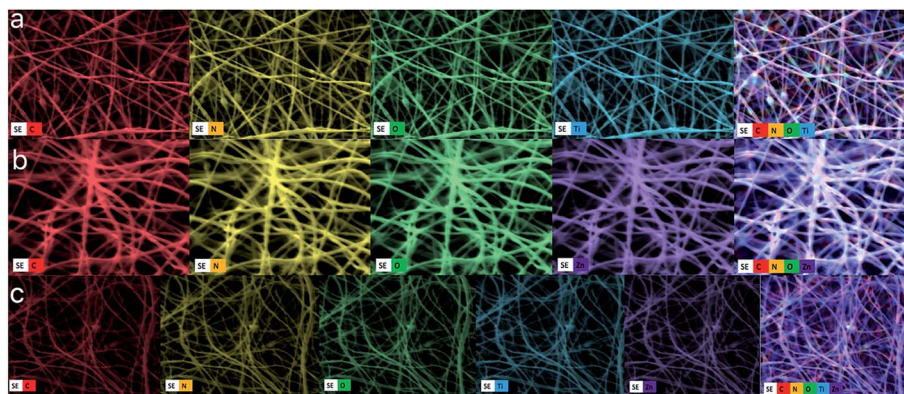


Fig. 5 Elemental mapping images of (a) PAN/TiO<sub>2</sub> nanofiber, (b) PAN/ZnO and (c) TiO<sub>2</sub>/ZnO/PAN nanofibers.

nanoparticles. The resulted aggregation of the nanoparticles in the middle of fibers owing to electrostatic repulsion since the TiO<sub>2</sub> with positive charges were repulsed by the positive charges on the surface of fibers and.<sup>35–37</sup> It is easy to observe that the sizes of the TiO<sub>2</sub> nanoparticles are about 5–50 nm, which is in good agreement with those measured by SEM above. Similarly, ZnO nanoparticles can be identified within PAN fibers as shown in Fig. 6c. It must be mentioned that the ZnO nanorods are aligned parallel to nanofiber axis, and their surfaces are relatively smoother with respect to PAN/TiO<sub>2</sub> nanofibers. In the case of TiO<sub>2</sub>/ZnO hybrid nanoparticles were used as filler in PAN nanofibers, the agglomerated TiO<sub>2</sub> nanoparticles are again

observed on the surface of nanofibers as seen in Fig. 6d. This suggests that TiO<sub>2</sub> nanoparticles with relatively smaller sizes agglomerated immediately after dispersion process in PAN solution and were spun as agglomerated structures due to the higher inner diameter of the needle (0.337 mm). TiO<sub>2</sub> nanoparticles tend to enlarge on the inside and surface of the hybrid nanofibers. Therefore, TiO<sub>2</sub> nanoparticles densely grown in the nanofiber are observed most likely due to an inhomogeneous and aggregation distribution of nanoparticle during electrospinning. Additionally, the HRTEM images of TiO<sub>2</sub>/ZnO/PAN hybrid nanofiber displays the existence of the ZnO nanorods and the TiO<sub>2</sub> nanoparticle in the nanofibers. Note that interplanar distance of 0.26 nm is close to the *d* spacing of the (002) planes of the hexagonal wurtzite structured of ZnO by confirming the good crystallinity as shown in Fig. 6e. The selected area electron diffraction (SAED) pattern (the inset in the upper left) shows a single crystalline of ZnO nanorod with the growth direction along (001). For TiO<sub>2</sub> nanoparticles, the interplanar distance of 0.32 nm is consistent with the *d* spacing of the (110) planes (Fig. 6f). The selected area electron diffraction (SAED) pattern (the inset in the upper left) if the TiO<sub>2</sub> nanosphere show that the nanoparticles exhibit good single crystalline and the basal plane of the rutile crystal structure with along the (001) axis.<sup>22</sup>

The presence of ZnO and TiO<sub>2</sub> nanoparticles within the electrospun PAN nanofibers, EDX analysis of hybrid nanofiber was also performed as presented in Fig. 7. The EDX spectrum demonstrates the fabricated hybrid nanofibers are mainly composed of carbon (C) nitrogen (N), oxygen (O), titanium (Ti), zinc (Zn) elements, the Au element originates in the conductive coating of the nanofibers. Ti, Zn, and Ti–Zn peaks were apparently observed from the EDX results for the PAN–TiO<sub>2</sub>, PAN–ZnO, and TiO<sub>2</sub>/ZnO/PAN nanofibers, respectively. The EDX results confirm the presence of nanoparticles on the nanofiber surface as well as the embedding of nanoparticles in PAN nanofiber.

FTIR analysis was also carried out to understand the structure of the electrospun hybrid nanocomposite fiber and the results are shown in Fig. 8. For the PAN electrospun nanofiber mat, the peaks at 2934 cm<sup>−1</sup> and 2873 cm<sup>−1</sup>, 1414 cm<sup>−1</sup>, and

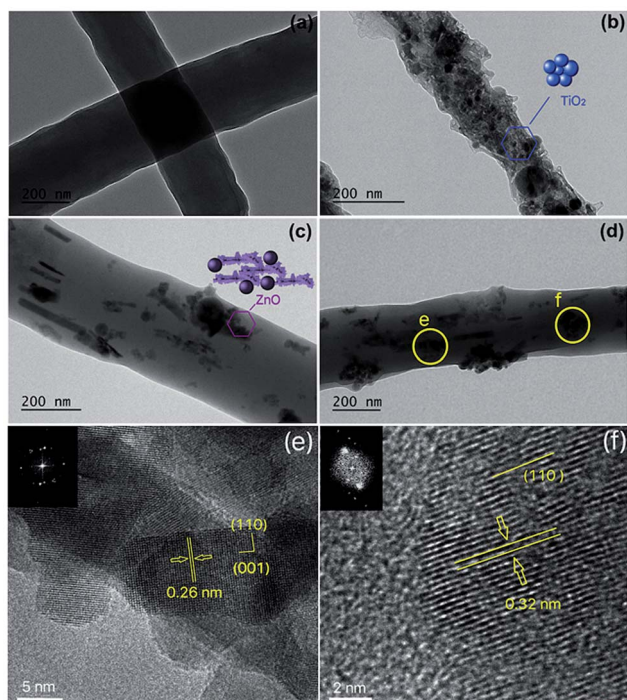


Fig. 6 TEM images of (a) pristine PAN nanofiber, (b) PAN/TiO<sub>2</sub> nanofiber, (c) PAN/ZnO and (d) TiO<sub>2</sub>/ZnO/PAN nanofibers, HR-TEM image of TiO<sub>2</sub>/ZnO/PAN hybrid nanofibers marked from yellow circle of (d) and the upper left inset the corresponding SAED pattern (e and f).





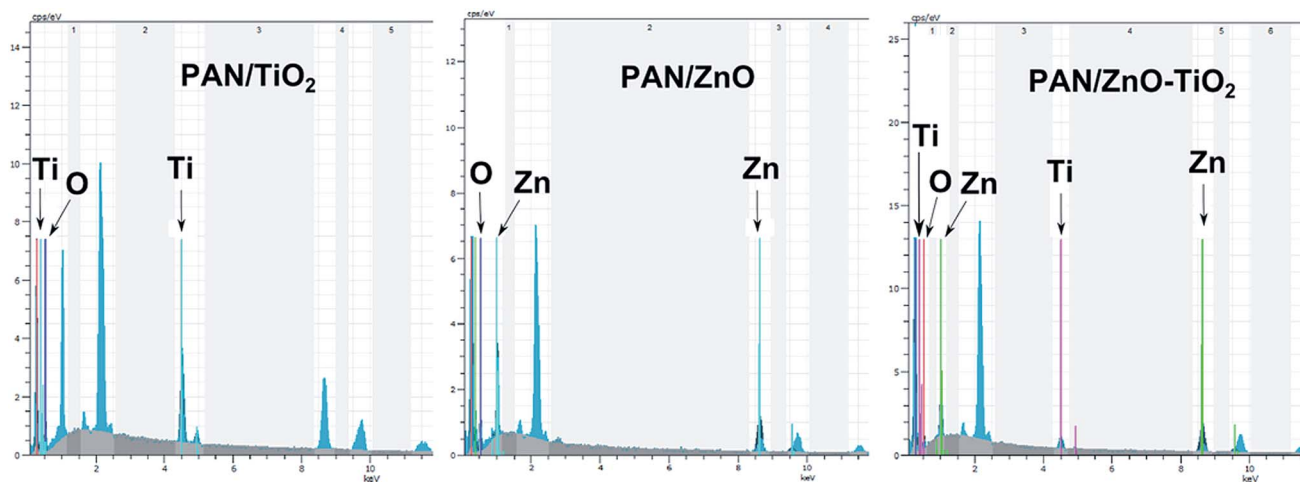


Fig. 7 EDX spectra of electrospun PAN based nanofibers containing  $\text{TiO}_2$ , ZnO and  $\text{TiO}_2$ -ZnO.

$1093\text{ cm}^{-1}$  are assigned to the aliphatic CH group vibration of different modes in OH,  $\text{CH}_2$  and CH, respectively.<sup>38</sup> The peaks at  $2241\text{ cm}^{-1}$  and  $1662\text{ cm}^{-1}$  related to the  $\text{C}\equiv\text{N}$  stretching and

$\text{C}=\text{O}$  stretching vibrations of the acrylamide, respectively.<sup>39</sup> Most important to the present discussion is the observation that compared with the nanoparticle-free nanofiber mats, the incorporation of nanoparticles results almost no differences of wavenumbers in the FTIR spectra but their intensities are slightly decreased. We confidently believe that the interaction between h-ZnO and r- $\text{TiO}_2$  nanoparticles embedded in PAN matrix is physical, not chemical.<sup>40</sup>

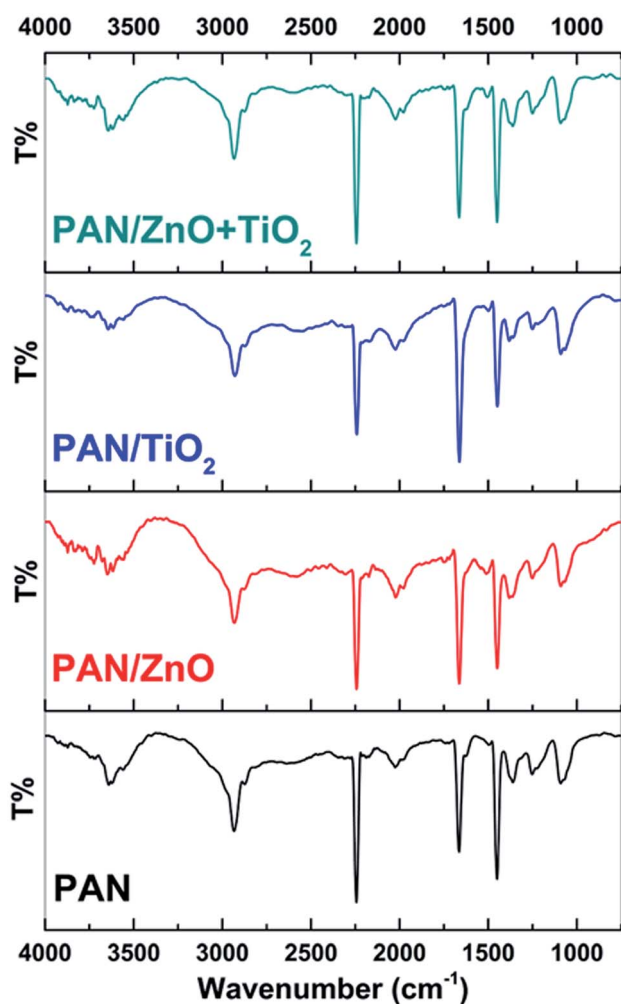


Fig. 8 FTIR spectra of pristine PAN nanofiber, PAN/ $\text{TiO}_2$  nanofiber, PAN/ZnO and PAN/ZnO- $\text{TiO}_2$  nanofibers.

### 3.2 Photocatalytic activity

Photocatalytic activities of the electrospun hybrid nanofibers were investigated by decolorization of malachite green dye solution under UV light source. Blank experiments such as without the nanofibers as the catalysts or light source indicate negligible decolorization of the dye.

The change in optical absorption spectra of MG dye by the electrospun hybrid nanofiber catalysts under UV light irradiation for different time intervals were shown in Fig. 9. It can be seen that the disappearance of the MG dye's characteristic peaks around 423 and 615 nm indicates that the MG dye has been decolorized that the dye has been degraded gradually with advancing time by the aid of electrospun hybrid nanofibers. The decolorization efficiencies are 93% and 91% in the presence of the electrospun PAN/ $\text{TiO}_2$  and PAN/ZnO nanofibers, respectively. In the same irradiation time, the bare PAN shows only 71% decolorization efficiency. It is found from photocatalytic experiments that the electrospun  $\text{TiO}_2$ /ZnO/PAN photocatalyst indicates better photocatalytic activity with 99% decolorization efficiency after 204 min. Fig. 10 shows the comparison of the decolorization rate of MG in the presence of electrospun  $\text{TiO}_2$ /ZnO/PAN nanofiber, pure PAN, PAN/ $\text{TiO}_2$ , and PAN/ZnO under UV light irradiation and dark conditions. Under dark conditions, MG dye was decolorized only between 6% and 11% in the presence of electrospun photocatalysts due to adsorption of the dye. After 60 min, MG dye was decolorized around 50% by using electrospun  $\text{TiO}_2$ /ZnO/PAN nanofibers under UV light irradiation. However, in the same conditions, decolorization of MG dye was reached only 29% in the presence



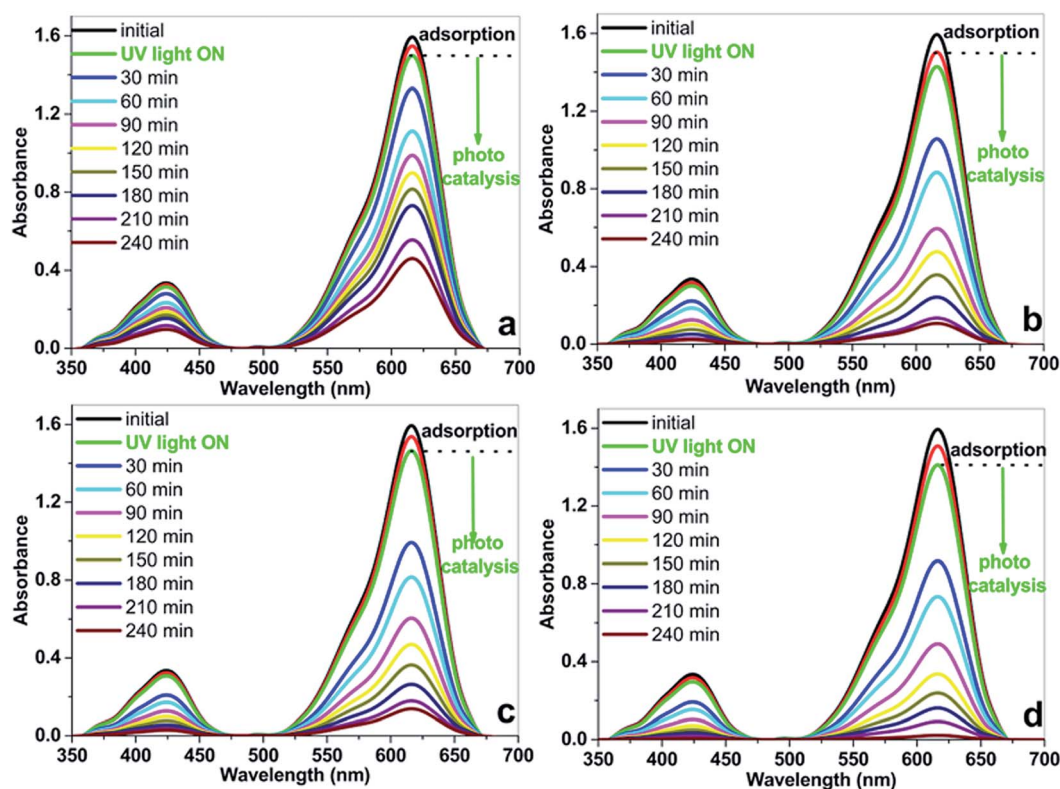


Fig. 9 The change in optical absorption spectra of MG dye by the electrospun hybrid nanofiber catalysts under UV light irradiation for different time intervals.

of pure PAN nanofiber. MG dye was decolorized completely by  $\text{TiO}_2/\text{ZnO}/\text{PAN}$  nanofiber after 240 min.

The reaction rate constant,  $k$  of the  $\text{TiO}_2/\text{ZnO}/\text{PAN}$  photocatalyst is  $0.01543 \text{ min}^{-1}$  which is approximately two times higher than the reaction rate constants of the bare PAN, PAN/ $\text{TiO}_2$  and PAN/ $\text{ZnO}$  nanofibers, respectively (Fig. 11). The results show that the PAN/ $\text{ZnO}/\text{TiO}_2$  photocatalyst illustrate superior photocatalytic activity for decolorization MG dye under UV light irradiation. The activity of electrospun PAN, PAN/ $\text{TiO}_2$ , PAN/ $\text{ZnO}$

and  $\text{TiO}_2/\text{ZnO}/\text{PAN}$  nanofiber can be evaluated by comparing the apparent rate constants ( $k_{\text{app}}$ ) as listed in Table 1.

The difference in photocatalytic properties between the nanofibers results from their different photocatalytic physics and photocatalytic chemistry. The photocatalytic physics mainly involves two physical factors. One is the absorption of light, and the other is the generation and recombination of the electrons and holes. The photocatalytic chemistry is mainly related to the

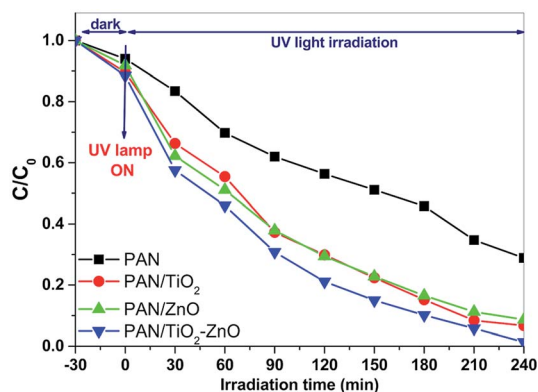


Fig. 10 Decolorization comparison of the MG with respect to time intervals over electrospun PAN, PAN/ $\text{TiO}_2$ , PAN/ $\text{ZnO}$  and  $\text{TiO}_2/\text{ZnO}/\text{PAN}$  photocatalyst under UV light (catalyst concentration:  $0.3 \text{ mg mL}^{-1}$ ; initial concentration of dye:  $1.0 \times 10^{-5} \text{ M}$ ).

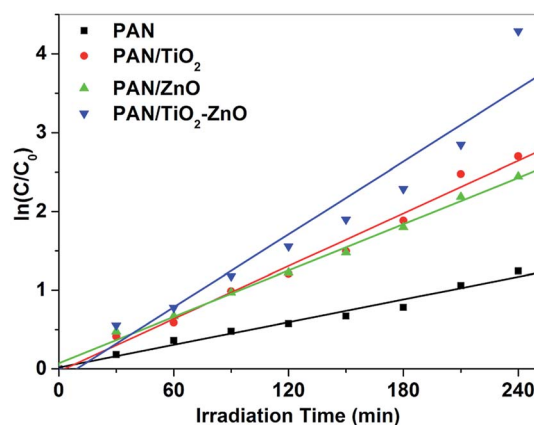


Fig. 11 Comparison of the apparent rate constants of electrospun PAN, PAN/ $\text{TiO}_2$ , PAN/ $\text{ZnO}$  and  $\text{TiO}_2/\text{ZnO}/\text{PAN}$  photocatalysts under UV light irradiation (catalyst concentration:  $0.3 \text{ mg mL}^{-1}$ ; initial concentration of dyes:  $1.0 \times 10^{-5} \text{ M}$ ).



**Table 1** Apparent rate constants ( $k_{app}$ ) of dyes degradation and linear regression coefficients from plot of  $\ln(C_0/C_t) = k_{app}t$  for of electrospun PAN, PAN/TiO<sub>2</sub>, PAN/ZnO and PAN/TiO<sub>2</sub>-ZnO photocatalysts under UV light irradiation after 210 min (catalyst concentration: 0.3 mg mL<sup>-1</sup>; initial concentration of dyes:  $1.0 \times 10^{-5}$  M)

	$k_{app}$ (min <sup>-1</sup> )	$R^2$
PAN	0.0048	0.9796
PAN/TiO <sub>2</sub>	0.01117	0.9875
PAN/ZnO	0.00982	0.9948
PAN/TiO <sub>2</sub> -ZnO	0.01543	0.9352

driving force of the electrons and holes transfer. Since the energy band gaps of TiO<sub>2</sub> and ZnO are similar, their differences in the driving forces of the electrons and holes transfer are negligible, suggesting that the photocatalytic chemistry has only fairly slight influence on their photocatalytic properties. On the other hand, numerous research endeavors have indicated that core-shell structures exhibit better photocatalytic performances by enhancing the photogenerated charge carriers.<sup>41–43</sup> Thereby, we believe the amorphous shell structure of the r-TiO<sub>2</sub> helps utilize the photogenerated charge carriers when it is in a form of thin shell on the crystalline r-TiO<sub>2</sub> core. However, the highest photocatalytic activity of the TiO<sub>2</sub>/ZnO/PAN nanocomposites is attributed to presence of both phases within the PAN matrix fiber with coupled mechanisms such as reduction of electron-hole pair recombination due to the stepwise energy level structure in the composite<sup>9,44,45</sup> and synergetic effect between hexagonal wurtzite ZnO and rutile TiO<sub>2</sub> phases.<sup>9</sup>

## 4. Conclusion

In briefly, we have adapted an associated process of arc-discharge and electrospinning techniques to fabricate PAN/TiO<sub>2</sub>, PAN/ZnO, and TiO<sub>2</sub>/ZnO/PAN hybrid nanofibers. Investigation demonstrates that TiO<sub>2</sub>, ZnO, and TiO<sub>2</sub>/ZnO nanoparticles have been favorably embedded within electrospun PAN nanofiber. The hybrid nanofibers possess specific surface area as well as being flexible in structure, resulting in a boost of photocatalytic efficiency. Also, TiO<sub>2</sub>/ZnO/PAN hybrid nanofibers have displayed better photocatalytic activity compared to the bare PAN nanofibers. Finally, we believe this strategy can be applied to remove of organic pollutants and water treatment due to their photocatalytic features with low energy consumption and flexible nature.

## Acknowledgements

The authors would like to thank State Planning Organization (DPT) and Selcuk University Scientific Research Council (BAP Project No. 15101009) for their financial support. Technical support from the Selcuk University Advanced Technology Research and Application Center is much appreciated.

## References

- 1 P. Bansal and D. Sud, *Sep. Purif. Technol.*, 2012, **85**, 112–119.

- 2 V. K. Gupta, R. Jain and S. Varshney, *J. Hazard. Mater.*, 2007, **142**, 443–448.
- 3 V. K. Gupta, A. Rastogi and A. Nayak, *J. Colloid Interface Sci.*, 2010, **342**, 135–141.
- 4 G. H. Chen, *Sep. Purif. Technol.*, 2004, **38**, 11–41.
- 5 A. Mittal, L. Kurup and V. K. Gupta, *J. Hazard. Mater.*, 2005, **117**, 171–178.
- 6 S. H. S. Chan, T. Y. Wu, J. C. Juan and C. Y. Teh, *J. Chem. Technol. Biotechnol.*, 2011, **86**, 1130–1158.
- 7 D. Alibegic, S. Tsuneda and A. Hirata, *Chem. Eng. Sci.*, 2001, **56**, 6195–6203.
- 8 F. X. L. I. Xamena, P. Calza, C. Lamberti, C. Prestipino, A. Damin, S. Bordiga, E. Pelizzetti and A. Zecchina, *J. Am. Chem. Soc.*, 2003, **125**, 2264–2271.
- 9 C. C. Pei and W. W. F. Leung, *Catal. Commun.*, 2013, **37**, 100–104.
- 10 N. J. Peill, L. Bourne and M. R. Hoffmann, *J. Photochem. Photobiol., A*, 1997, **108**, 221–228.
- 11 S. Livraghi, K. Elghniji, A. M. Czoska, M. C. Paganini, E. Giamello and M. Ksibi, *J. Photochem. Photobiol., A*, 2009, **205**, 93–97.
- 12 W. Liu, S. F. Chen, S. J. Zhang, W. Zhao, H. Y. Zhang and X. L. Yu, *J. Nanopart. Res.*, 2010, **12**, 1355–1366.
- 13 X. L. Ren, P. Z. Ying, Z. B. Yang, M. H. Shang, H. L. Hou and F. M. Gao, *RSC Adv.*, 2015, **5**, 16361–16367.
- 14 A. M. Azad, S. A. Akbar, L. B. Younkman and M. A. Alim, *J. Am. Ceram. Soc.*, 1994, **77**, 3145–3152.
- 15 T. Ohno, K. Tokieda, S. Higashida and M. Matsumura, *Appl. Catal., A*, 2003, **244**, 383–391.
- 16 H. W. Cen, X. J. Li, M. X. He, S. J. Zheng and M. Z. Feng, *Chemosphere*, 2006, **62**, 810–816.
- 17 B. Haspulat, A. Gulce and H. Gulce, *J. Hazard. Mater.*, 2013, **260**, 518–526.
- 18 D. Zhang, A. B. Karki, D. Rutman, D. R. Young, A. Wang, D. Cocke, T. H. Ho and Z. H. Guo, *Polymer*, 2009, **50**, 4189–4198.
- 19 J. H. Zhu, S. Y. Wei, X. L. Chen, A. B. Karki, D. Rutman, D. P. Young and Z. H. Guo, *J. Phys. Chem. C*, 2010, **114**, 8844–8850.
- 20 C. Y. Su, Y. F. Tong, M. Y. Zhang, Y. Zhang and C. L. Shao, *RSC Adv.*, 2013, **3**, 7503–7512.
- 21 J. S. Im, M. Il Kim and Y. S. Lee, *Mater. Lett.*, 2008, **62**, 3652–3655.
- 22 A. Avci, V. Eskizeybek, H. Gulce, B. Haspulat and O. S. Sahin, *Appl. Phys. A: Mater. Sci. Process.*, 2014, **116**, 1119–1125.
- 23 V. Eskizeybek, F. Sari, H. Gulce, A. Gulce and A. Avci, *Appl. Catal., B*, 2012, **119**, 197–206.
- 24 S. Sonmezoglu, V. Eskizeybek, A. Toumiat and A. Avci, *J. Alloys Compd.*, 2014, **586**, 593–599.
- 25 F. Ozel, M. Kus, A. Yar, E. Arkan, M. Can, A. Aljabour, N. M. Varal and M. Ersoz, *J. Mater. Sci.*, 2015, **50**, 777–783.
- 26 F. Ozel, M. Kus, A. Yar, E. Arkan, M. Z. Yigit, A. Aljabour, S. Buyukcelebi, C. Tozlu and M. Ersoz, *Mater. Lett.*, 2015, **140**, 23–26.
- 27 B. G. Colvin and P. Storr, *Eur. Polym. J.*, 1974, **10**, 337–340.
- 28 X. D. Liu and W. Ruland, *Macromolecules*, 1993, **26**, 3030–3036.





- 29 Y. Y. Chen, C. C. Kuo, B. Y. Chen, P. C. Chiu and P. C. Tsai, *J. Polym. Sci., Part B: Polym. Phys.*, 2015, **53**, 262–269.
- 30 D. D. Lin, H. Wu, R. Zhang and W. Pan, *Chem. Mater.*, 2009, **21**, 3479–3484.
- 31 A. A. Ashkarran, A. I. Zad, M. M. Ahadian and S. A. M. Ardakani, *Nanotechnology*, 2008, **19**, 195709–195715.
- 32 M. C. Medina, D. Rojas, P. Flores, E. Perez-Tijerina and M. F. Melendrez, *J. Appl. Polym. Sci.*, 2016, **133**, 43631–43638.
- 33 X. G. Liu, Y. P. Sun, C. Feng, C. G. Jin and W. H. Li, *Appl. Surf. Sci.*, 2013, **280**, 132–137.
- 34 S. J. Fang, W. Wang, X. L. Yu, H. Xu, Y. Zhong, X. F. Sui, L. P. Zhang and Z. P. Mao, *Mater. Lett.*, 2015, **143**, 120–123.
- 35 H. C. Yu, Z. B. Jiao, H. Y. Hu, G. X. Lu, J. H. Ye and Y. P. Bi, *CrystEngComm*, 2013, **15**, 4802–4805.
- 36 C. Prahsarn, W. Klinsukhon and N. Roungpaisan, *Mater. Lett.*, 2011, **65**, 2498–2501.
- 37 C. S. Sharma, A. Sharma and M. Madou, *Langmuir*, 2010, **26**, 2218–2222.
- 38 I. M. Alarifi, A. Alharbi, W. S. Khan, A. Swindle and R. Asmatulu, *Materials*, 2015, **8**, 7017–7031.
- 39 S. Dalton, F. Heatley and P. M. Budd, *Polymer*, 1999, **40**, 5531–5543.
- 40 J. Shang, M. Chai and Y. F. Zhu, *J. Solid State Chem.*, 2003, **174**, 104–110.
- 41 S. Lee, K. Lee, W. D. Kim, S. Lee, D. J. Shin and D. C. Lee, *J. Phys. Chem. C*, 2014, **118**, 23627–23634.
- 42 J. Li, C. H. Liu, X. Li, Z. Q. Wang, Y. C. Shao, S. D. Wang, X. L. Sun, W. F. Pong, J. H. Guo and T. K. Sham, *Chem. Mater.*, 2016, **28**, 4467–4475.
- 43 Y. Q. Yang, G. Liu, J. T. S. Irvine and H. M. Cheng, *Adv. Mater.*, 2016, **28**, 5850–5856.
- 44 C. Karunakaran, G. Abiramasundari, P. Gomathisankar, G. Manikandan and V. Anandi, *Mater. Res. Bull.*, 2011, **46**, 1586–1592.
- 45 F. X. Xiao, *ACS Appl. Mater. Interfaces*, 2012, **4**, 7054–7062.

